

## Full length article

# Reasons for the superior mechanical properties of medium-entropy CrCoNi compared to high-entropy CrMnFeCoNi

G. Laplanche <sup>a,\*</sup>, A. Kostka <sup>a,b</sup>, C. Reinhart <sup>a</sup>, J. Hunfeld <sup>a</sup>, G. Eggeler <sup>a</sup>, E.P. George <sup>a,b</sup><sup>a</sup> Institut für Werkstoffe, Ruhr-Universität Bochum, D-44801, Bochum, Germany<sup>b</sup> Materials Research Department and Center for Interface Dominated Materials (ZGH), Ruhr-University Bochum, Germany

## ARTICLE INFO

## Article history:

Received 15 September 2016

Received in revised form

7 February 2017

Accepted 12 February 2017

Available online 13 February 2017

## Keywords:

Medium-entropy and high-entropy alloys

Strain hardening

Shockley partial dislocations

Stacking fault energy

Deformation twinning

## ABSTRACT

The tensile properties of CrCoNi, a medium-entropy alloy, have been shown to be significantly better than those of CrMnFeCoNi, a high-entropy alloy. To understand the deformation mechanisms responsible for its superiority, tensile tests were performed on CrCoNi at liquid nitrogen temperature (77 K) and room temperature (293 K) and interrupted at different strains. Microstructural analyses by transmission electron microscopy showed that, during the early stage of plasticity, deformation occurs by the glide of  $1/2<110>$  dislocations dissociated into  $1/6<112>$  Shockley partials on {111} planes, similar to the behavior of CrMnFeCoNi. Measurements of the partial separations yielded a stacking fault energy of  $22 \pm 4 \text{ mJ m}^{-2}$ , which is ~25% lower than that of CrMnFeCoNi. With increasing strain, nanotwinning appears as an additional deformation mechanism in CrCoNi. The critical resolved shear stress for twinning in CrCoNi with 16  $\mu\text{m}$  grain size is  $260 \pm 30 \text{ MPa}$ , roughly independent of temperature, and comparable to that of CrMnFeCoNi having similar grain size. However, the yield strength and work hardening rate of CrCoNi are higher than those of CrMnFeCoNi. Consequently, the twinning stress is reached earlier (at lower strains) in CrCoNi. This in turn results in an extended strain range where nanotwinning can provide high, steady work hardening, leading to the superior mechanical properties (ultimate strength, ductility, and toughness) of medium-entropy CrCoNi compared to high-entropy CrMnFeCoNi.

© 2017 The Author(s). Published by Elsevier Ltd. This is an open access article under the CC BY 4.0 license (<http://creativecommons.org/licenses/by/4.0/>).

## 1. Introduction

Despite what is often assumed in the high-entropy alloy (HEA) literature, and sometimes explicitly stated [e.g. Ref. [1], that configurational entropy (compositional complexity) correlates directly with the degree of solid solution strengthening, there is actually scant evidence to support this notion. In most papers where superior mechanical properties are attributed to solid solution strengthening from multiple principal elements, the results are clouded by the presence of second phases. This complicates mechanistic interpretation because of the introduction of "composite" effects. In the case of complex solid solutions with face-centered cubic (FCC) structures, Gali and George [2] first showed that increasing the number of constituent elements from four in the CrFeCoNi medium-entropy alloy (MEA), to five in the CrMnFeCoNi HEA, had negligible effect on the degree of solid solution

strengthening as evidenced by their similar yield and ultimate tensile strengths. Subsequent studies [3,4] on a family of single-phase FCC alloys, including several MEAs comprising the elements present in the CrMnFeCoNi HEA, found no systematic correlation between mechanical properties and number of alloying elements (i.e., configurational entropy). For example, it was found that the ternary CrCoNi had the highest yield strength and hardness, higher than those of the quaternary and quinary alloys containing more elements. Additionally, alloys with the same configurational entropy had different strengths (e.g., FeNi was significantly stronger than FeCo, and CrCoNi was significantly stronger than MnFeNi). Interestingly, similar alloying trends were noted also for ductility, with the stronger alloys generally being the more ductile [4]. Consistent with the fact that the CrCoNi MEA [4] has higher strength and ductility than the CrMnFeCoNi HEA [2,5], it has also been demonstrated that the fracture toughness of the MEA [6] is higher than that of the HEA [7].

The microstructural aspects of plasticity in the CrMnFeCoNi HEA and its non-equiautomic counterparts have been extensively investigated during the past three years [5,8–23]. Detailed analysis of

\* Corresponding author.

E-mail address: [guillaume.laplanche@rub.de](mailto:guillaume.laplanche@rub.de) (G. Laplanche).

microstructure evolution with strain, coupled with determination of the critical stress for twinning, has greatly improved our understanding of work hardening mechanisms and reasons for the increase in strength and ductility of this HEA with decreasing temperature [16]. In contrast, despite having superior mechanical properties, the CrCoNi MEA has received little attention so far. Consequently, the microstructural origins of its high strength and ductility remain unclear. Even basic features of its plastic deformation behavior including slip planes, Burgers vectors, and dislocation dissociations, have not been reported. In addition, its stacking fault energy has not been determined. Finally, basic questions about its twinning behavior remain unanswered, including: (1) when does twinning start at 293 K and 77 K? (2) Is there a critical stress for twinning? (3) Does the twinning stress depend on temperature? (4) How does its magnitude compare to that of the CrMnFeCoNi HEA? To answer these questions and shed light on the micromechanisms of deformation and fracture in the CrCoNi MEA, we interrupted mechanical tests after several different strains and analyzed the microstructures by transmission electron microscopy (TEM). Its deformation mechanisms were then compared to those of CrMnFeCoNi to develop a better understanding of the superior mechanical properties of CrCoNi.

## 2. Experimental methods

### 2.1. Processing

An equiatomic CrCoNi alloy weighing 2.1 kg was produced by vacuum induction melting using pure elements (purity  $\geq 99.9$  wt%) as starting materials. Melting was performed in a Leybold Heraeus IS 1/III vacuum induction furnace operating at 5–20 kW. Prior to melting, the furnace chamber was evacuated to 3 mbar and then backfilled with Ar (purity, 99.998 vol%) to a pressure of 500 mbar. The raw materials were melted in a MgO crucible and poured into a zirconia-slurry coated cylindrical steel mold having a diameter of 45 mm and height of 160 mm. These processes are similar to those used for the melting and casting of the CrMnFeCoNi HEA [16,24,25]. The cast ingot was turned on a lathe to reduce its diameter from 45 mm to 40 mm, sealed in an evacuated quartz tube, and homogenized at 1473 K for 48 h. After homogenization, the quartz tube was taken out of the furnace and allowed to cool in air to room temperature, following which the alloy was removed from the quartz tube. The homogenized ingot was swaged using a four-die rotary swaging machine of type HMP R6-4-120-21S (HMP Umformtechnik GmbH, Pforzheim, Germany). In seven steps, its diameter was reduced from 40 to 16.5 mm (total true strain of ~1.8). After the final reduction, the swaged material was recrystallized for 1 h at 1173 K followed by air-cooling. Swaging was used for deformation processing of the present CrCoNi alloy since that was how we produced the CrMnFeCoNi alloy in our previous study [16]. This facilitated direct comparison of their mechanical properties.

### 2.2. Mechanical testing

From the recrystallized rod, rectangular dog-bone shaped tensile specimens (gauge length, 20 mm) were fabricated by electrical discharge machining such that their loading axes were parallel to the rod axis. Before the tensile tests, all faces of the specimens were ground to 1000 grit finish using SiC paper resulting in a final thickness of ~1.2 mm and a gauge section of ~4.8 mm<sup>2</sup>. Tensile tests were performed at an engineering strain rate of  $10^{-3}$  s<sup>-1</sup> in a Zwick/Roell test rig of type Z100 at 77 K and 293 K. The room-temperature (293-K) tests were conducted in ordinary ambient air while the 77-K tests utilized a custom-built chamber filled with liquid nitrogen into which the specimens and grips were fully immersed. At 293 K,

strains were measured with an extensometer attached to the gauge section and engineering stress-strain curves were obtained from these strains and the output from the load cell. At 77 K, our extensometer could not be used, so strains were determined indirectly from crosshead displacements that were corrected using the following procedure. First, 20 Vickers microindents spaced 1 mm apart were made along the gauge lengths of several tensile specimens using a force of 3.9 N. The specimens were tensile tested to different stress levels, unloaded, and the plastic strains in their gauge sections determined by averaging the change in spacing of the indents. In this way, a full engineering stress-strain curve was constructed from the different interrupted tests. This calibration curve was used to correct the crosshead displacements and obtain engineering stress-strain curves for the specimens tested at 77 K. For both test temperatures, true stress-strain curves were obtained from the engineering stress-strain curves assuming constancy of volume during plastic deformation.

### 2.3. Microstructural characterization

Longitudinal sections were cut from the recrystallized alloy, ground and polished with SiC abrasive papers down to a grit size of 8  $\mu$ m and then with diamond suspensions down to 1  $\mu$ m. Final polishing was performed with a vibratory polisher (Buehler Vibromet 2) and colloidal silica having a particle size of 0.06  $\mu$ m; long polishing times up to 48 h were employed to minimize residual deformation near the surface.

Phase characterization was carried out by X-ray diffraction using a PANalytical X'Pert Pro MRD diffractometer equipped with a 4-bounce germanium (220) monochromator (Cu K $\alpha$  radiation  $\lambda = 0.154$  nm;  $2\theta$  range from 40° to 120°; step size  $\Delta 2\theta = 0.006^\circ$ ; integration time 280 s).

Chemical composition of the swaged alloy was determined at a commercial laboratory (Revierlabor GmbH, Essen, Germany), which is the same one that we had used previously [36]. Metallic elements were analyzed by X-ray fluorescence analysis (XRFA), oxygen by carrier gas hot extraction, and carbon and sulfur by the combustion IR absorption method. Additional chemical analyses were performed by us using energy dispersive X-ray spectroscopy (EDX) at an accelerating voltage of 25 kV and a working distance of 8.5 mm in a scanning electron microscope (SEM) of type Leo 1530 VP. Five locations, each covering an area of 400  $\mu$ m  $\times$  300  $\mu$ m and spaced 2 mm apart between the center and the outer edge of the recrystallized rod were analyzed by EDX to check whether the recrystallized alloys are chemically homogeneous.

Texture was determined by electron backscatter diffraction (EBSD) in a SEM of type Quanta FEI 650 ESEM equipped with a Hikari XP camera (EDAX, AMETEK) at an accelerating voltage of 30 kV, a working distance of 11–15 mm and step sizes between 0.3 and 1  $\mu$ m. Pattern analysis was performed using the TSL OIM Analysis software (version 6.2.0). As rotary swaging is axisymmetric, the texture of the recrystallized rod is represented by an inverse pole figure (IPF) along a direction parallel to the rod axis. The IPF was calculated using the harmonic expansion method up to a series expansion degree of 22 and a Gaussian half width of 5° without imposing any sample symmetry. Texture intensities are given as multiples of a random orientation distribution (m.r.d.).

Mean grain size was determined with the Heyn linear intercept method (ASTM E112-10) using four equidistant and parallel lines of identical length per micrograph. Annealing twin boundaries were not counted as grain boundaries. Five backscatter electron micrographs, taken at locations spaced 2 mm apart between the center and the outer surface of the recrystallized rod were used for the determination of the mean grain size. Using this method, the determination of the mean grain size involved about 1000

intercepts.

To investigate microstructure evolution during tensile straining, slices for TEM were cut from the gauge sections of deformed tensile specimens. These slices were ground to a thickness of 90  $\mu\text{m}$  using 600-grit SiC paper. TEM foils were then prepared by double-jet electrochemical thinning at 20 V using an electrolyte consisting of 70 vol% of methanol, 20 vol% of glycerine, and 10 vol% perchloric acid at 253 K. TEM analyses were performed on a Tecnai Supertwin F20 G2 instrument operating at 200 kV.

#### 2.4. Dislocation analysis and measurement of the stacking fault energy (SFE)

To determine the operative slip systems and the SFE of the CrCoNi alloy, 3 mm diameter TEM disks need to be extracted from strained specimens at 45° to the loading axis. For geometrical reasons, such disks could not be obtained from the gauge sections ( $1.2 \times 4 \times 20 \text{ mm}^3$ ) of our tensile specimens. Therefore, additional cylindrical specimens with a length of 10 mm and a diameter of 4 mm were deformed in compression at 293 K to ~4% strain at an engineering strain rate of  $10^{-3} \text{ s}^{-1}$ . The stress-strain curves in compression and tension are identical during the early stage of plasticity, i.e. they exhibit the same yield stress and work hardening rate up to 4% strain. Slices were cut from the compression specimen at 45° to the loading axis and TEM specimens were prepared as described in section 2.3. To determine the Burgers vectors of the dislocations introduced during compression,  $\mathbf{g} \cdot \mathbf{b}$  analysis was carried out. In the following,  $\mathbf{b}$  is the Burgers vector of a full dislocation and  $\mathbf{b}_{\mathbf{p}1}$  and  $\mathbf{b}_{\mathbf{p}2}$  are the Burgers vectors of the corresponding Shockley partials.

Measurements of dissociation widths were performed on partial dislocations lying on {111} planes nearly parallel to the TEM foil using the <111> zone-axis nearly perpendicular to the TEM foil. Under these conditions, three  $\mathbf{g}$  vectors of type <110> are available, e.g. [2 0 2], [2 2 0] and [0 2 2] for the [111] zone axis. Weak beam was employed using the g(3g) configuration leading to  $\mathbf{g} \cdot \mathbf{b} \leq 2$ , an excitation distance  $\xi_g \sim 100 \text{ nm}$  determined using the large angle convergent beam technique [26–28] and an excitation error  $s_g \sim 0.15 \text{ nm}^{-1}$  calculated using

$$s_g = \frac{1}{2}(n - 1) |\mathbf{g}|^2 \lambda \quad (1)$$

where  $\lambda$  is the electron wavelength and  $n = 3$  for g(3g) [28]. To ensure that the image peak position of the partials is insensitive to foil thickness and dislocation depth, Cockayne [29] has shown that the parameter  $w = s_g \xi_g$  should fulfill the requirement that  $w \geq 5$ , which is the case in the present study since  $w = 15$ . Regarding the resolution (image width) of the partials, Cockayne [30] suggested using an excitation error  $s_g \geq 0.2 \text{ nm}^{-1}$  to obtain an image half-width (or full-width at half-height) of an edge partial of 2.5 nm (the image of an edge dislocation is 1.75 times broader than that of a screw [31]). Note that edge and screw here refer to the character of the full dislocation. Historically, Cockayne's experiments were performed using an acceleration voltage of 100 kV in the TEM, which yields a value of  $s_g = 0.2 \text{ nm}^{-1}$  for copper. In the present study the acceleration voltage was 200 kV, making  $s_g$  closer to  $0.15 \text{ nm}^{-1}$ , which results in a resolution of 3.3 nm for an edge partial, i.e., partials spaced less than 3.3 nm apart cannot be resolved. While this slight decrease in resolution may be problematic in FCC materials with a high SFE like copper or nickel ( $\text{SFE} > 40 \text{ mJ m}^{-2}$ ), it does not impose a significant burden in materials with a low SFE like the CrCoNi alloy studied here. Dissociation widths were measured at locations spaced 30 nm apart along extended, straight sections of isolated dislocations in relatively

thick areas (foil thickness: 260 nm) to minimize effects of image forces.

Because the strain field in regions between the Shockley partials is different from that outside the dissociated pair, one of the two partials appears brighter than the other when using weak beam diffraction imaging. Moreover, the image peaks of the partials are not equidistant from their respective cores, i.e., the observed dissociation width  $d_{\text{obs}}$  differs from the actual spacing between partials,  $d_{\text{act}}$ , and the following correction has to be applied to determine the actual dissociation width [30]:

$$d_{\text{act}} = \sqrt{d_{\text{obs}}^2 - \frac{4}{a b} + \frac{b - a}{a b}} \quad (2)$$

$$a = \frac{-s_g}{\frac{\mathbf{g}}{2\pi} \cdot (\mathbf{b}_{\mathbf{p}1} + \frac{\mathbf{b}_{\mathbf{p}1,e}}{2(1-\nu)})} \quad (3)$$

$$b = \frac{-s_g}{\frac{\mathbf{g}}{2\pi} \cdot (\mathbf{b}_{\mathbf{p}2} + \frac{\mathbf{b}_{\mathbf{p}2,e}}{2(1-\nu)})} \quad (4)$$

where  $\nu$  is Poisson's ratio (0.3 for the CrCoNi alloy [4]), and  $\mathbf{b}_{\mathbf{p}1}$ ,  $\mathbf{b}_{\mathbf{p}2}$  and  $\mathbf{b}_{\mathbf{p}1,e}$ ,  $\mathbf{b}_{\mathbf{p}2,e}$  are the Burgers vectors of the partial dislocations and their edge components, respectively, which can be calculated from the lattice parameter determined in section 3.1.

The equilibrium spacing between Shockley partials is the result of two opposing forces. On the one hand, the partials want to be as close as possible to minimize the width and thus energy of the stacking fault, while on the other they want to be as far apart as possible to minimize the repulsive elastic interaction between the dislocations. Assuming isotropic elasticity, the SFE can be calculated from the dissociation width using

$$\text{SFE} = \frac{G b_p^2}{8 \pi d_{\text{act}}} \left( \frac{2 - \nu}{1 - \nu} \right) \left( 1 - \frac{2 \nu \cos(2\beta)}{2 - \nu} \right) \quad (5)$$

where  $G$  is the shear modulus (87 GPa for the CrCoNi alloy [4]),  $\beta$  is the angle between the dislocation line and the Burgers vector of the full dislocation, and  $b_p$  is the magnitude of the Burgers vector of the partials (0.146 nm, derived from the measured lattice parameter in section 3.1).

## 3. Results and discussion

### 3.1. Crystallography, chemical composition, microstructure and texture

An X-ray diffraction pattern taken on a longitudinal section of the swaged and recrystallized rod is shown in Fig. 1. All diffraction peaks can be indexed assuming a single FCC phase with a lattice parameter  $a = 0.3567 \text{ nm}$ .

As shown in Table 1, the chemical composition of the CrCoNi alloy determined by XRFA, 32.53Cr-33.30Co-32.85Ni (at.%), is close to the targeted equiatomic composition. Additionally, EDX measurements performed at different locations (as described in section 2.3) revealed a uniform, nearly equiatomic chemical composition. The concentrations of the impurity elements, C, O, and S, are all relatively low. Similar results were previously reported for the CrMnFeCoNi alloy [36] and are presented in Table 1 for comparison. Based on these results, it is unlikely that the superior mechanical properties of the CrCoNi MEA are due to deviations from the equiatomic composition or major differences in the impurity concentrations.

The microstructure and the texture of the fully recrystallized

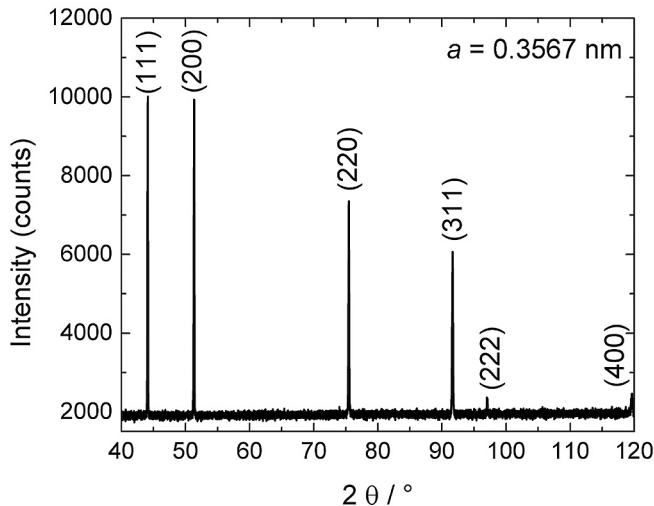


**Fig. 1.** X-ray diffraction pattern of the recrystallized CrCoNi alloy indexed as single-phase FCC with lattice parameter  $a = 0.3567 \text{ nm}$ .

**Table 1**

Chemical composition (in at.%) of the CrCoNi medium-entropy alloy. For comparison, the chemical composition (in at.%) of the CrMnFeCoNi high-entropy alloy taken from Ref. [36] is also given. The precision of the values is 0.02% and 0.005% for metallic and non-metallic elements, respectively.

Alloy	Cr	Mn	Fe	Co	Ni	C	O	S
CrCoNi	32.53	0.09	0.95	33.30	32.85	0.019	0.226	0.004
CrMnFeCoNi	19.41	20.10	20.56	20.26	19.58	0.051	0.033	0.009

CrCoNi were characterized by EBSD. Fig. 2a shows a high magnification backscatter micrograph in which the longitudinal axis of the swaged rods is indicated by the white arrow in the upper right corner. An equiaxed grain structure can be seen along with a few dark regions that are elongated along the rod axis (see upper left corner in Fig. 2a). EDX analysis revealed that these dark regions are oxide particles. Additional analyses (not shown here) revealed that these oxides formed during melting and casting and their volume fraction did not change after thermomechanical processing. However, they fracture during swaging causing them to appear as stringers aligned parallel to the deformation direction. Using image

analysis software their surface area fraction, which does not vary along the radius, was determined to be  $0.004 \pm 0.001$ . Fig. 2b is a grain orientation map with an overlaid image quality map where the individual crystallites are colored according to their crystallographic orientation relative to the rod axis (as shown in the upper right corner of Fig. 2a). In Fig. 2b, equiaxed grains containing several  $\Sigma 3$  annealing twins can be observed. Their density was determined to be  $2.5 \pm 0.1$  twins per grain using the procedure described in Ref. [32]. The grain size is uniform along the radius of the recrystallized rod and has a mean value of  $16 \pm 5 \mu\text{m}$ . The IPF in Fig. 2c shows that the texture along the rod axis is almost random, with a slight  $<111>$  and a weak  $<100>$  fiber texture, as indicated by a maximum pole intensity that is ~2.3 times random. This slight texture obtained after swaging and recrystallization is typical of FCC metals and alloys [24,33–36]. Finally, as XRD and EBSD are relatively coarse-scale observations that could miss small second-phase particles, extensive TEM analysis was carried out to look for precipitates. Fig. 3a is a bright field (BF) image taken at low magnification showing the absence of any second phase particles at the grain boundaries or within the grains. The white dashed circle in Fig. 3a indicates the selected area contributing to the selected area diffraction (SAD) pattern shown in Fig. 3b. No additional diffraction spots other than those of the FCC lattice can be seen, consistent with the absence of secondary phases. Additionally, the as-recrystallized alloy exhibits a very low dislocation density as shown in Fig. 3a. Similar results were obtained at all other locations examined. In summary, the CrCoNi MEA investigated here is single-phase FCC, with an equiaxed nearly random grain structure, a grain size of approximately  $16 \mu\text{m}$ , and low starting dislocation density.

### 3.2. Tensile properties

The true stress – true strain response of the polycrystalline CrCoNi alloy tensile tested to fracture at 77 K and 293 K is shown in Fig. 4a (arrowed curves). Also shown are stress-strain curves from several additional tests that were interrupted before failure and unloaded after reaching different stress levels (the corresponding engineering stress-strain curves are not shown in the interest of saving space). As the test temperature is decreased from 293 K to 77 K, the yield strength  $\sigma_y$  increases from  $360 \pm 10 \text{ MPa}$  to  $560 \pm 20 \text{ MPa}$  and the ultimate tensile strength  $\sigma_{uts}$  increases from ~870 MPa to ~1230 MPa. Additionally, the tensile ductility (strain to failure) increases from ~38% at 293 K to ~45% at 77 K.

The derivative of true stress with respect to true strain,  $d\sigma/d\varepsilon$ ,

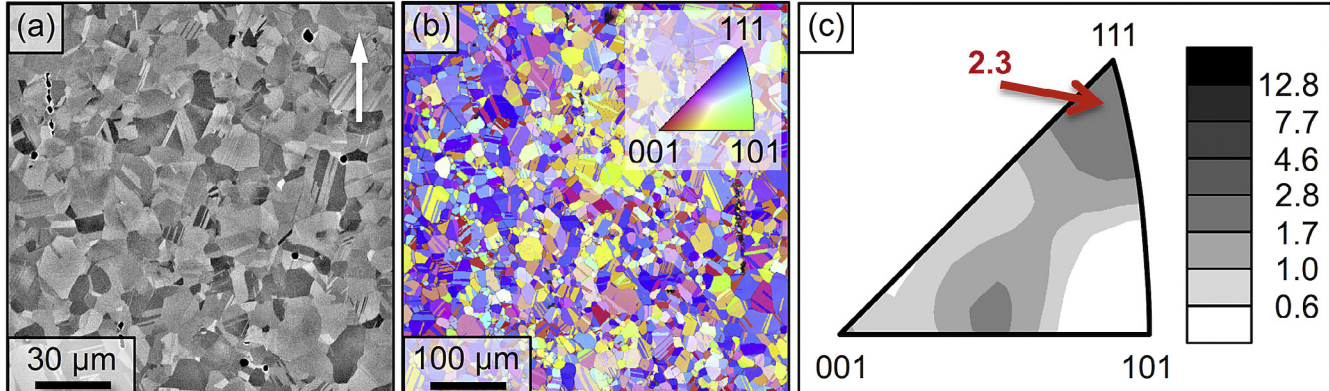


**Fig. 2.** Representative microstructure of the recrystallized CrCoNi alloy. (a) SEM backscatter micrograph with white arrow in the upper right corner indicating the axis of the swaged rod, (b) color-coded grain orientation map on a plane parallel to the deformation direction where the colors indicate the crystal orientations (see stereographic triangle in the upper right corner), (c) inverse pole figure showing weak texture parallel to the rod axis (texture is shown as multiples of random orientation, with the red arrow indicating a maximum of 2.3 times random orientation). (For interpretation of the references to colour in this figure legend, the reader is referred to the web version of this article.)

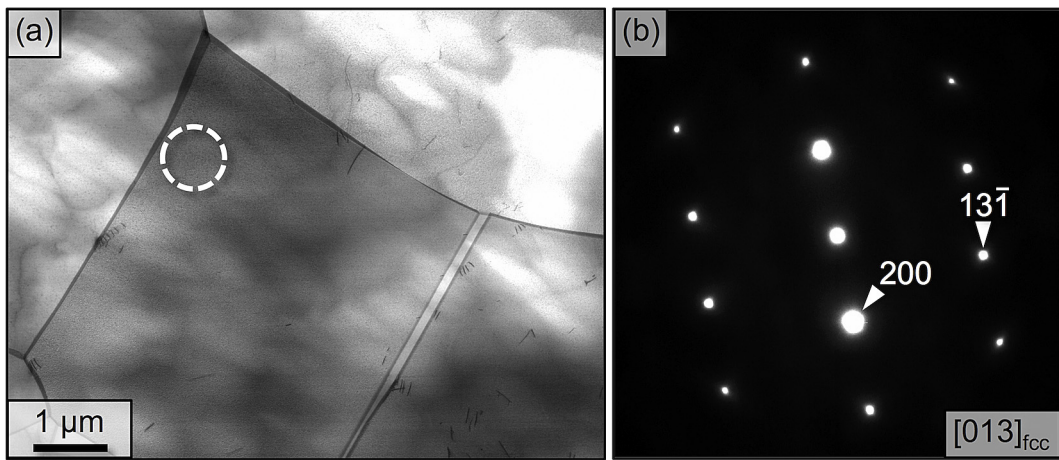


**Fig. 3.** Representative TEM micrograph of the CrCoNi alloy in the as-recrystallized state. (a) High magnification BF image. (b) Diffraction pattern from the selected area highlighted by the dashed circle in (a).

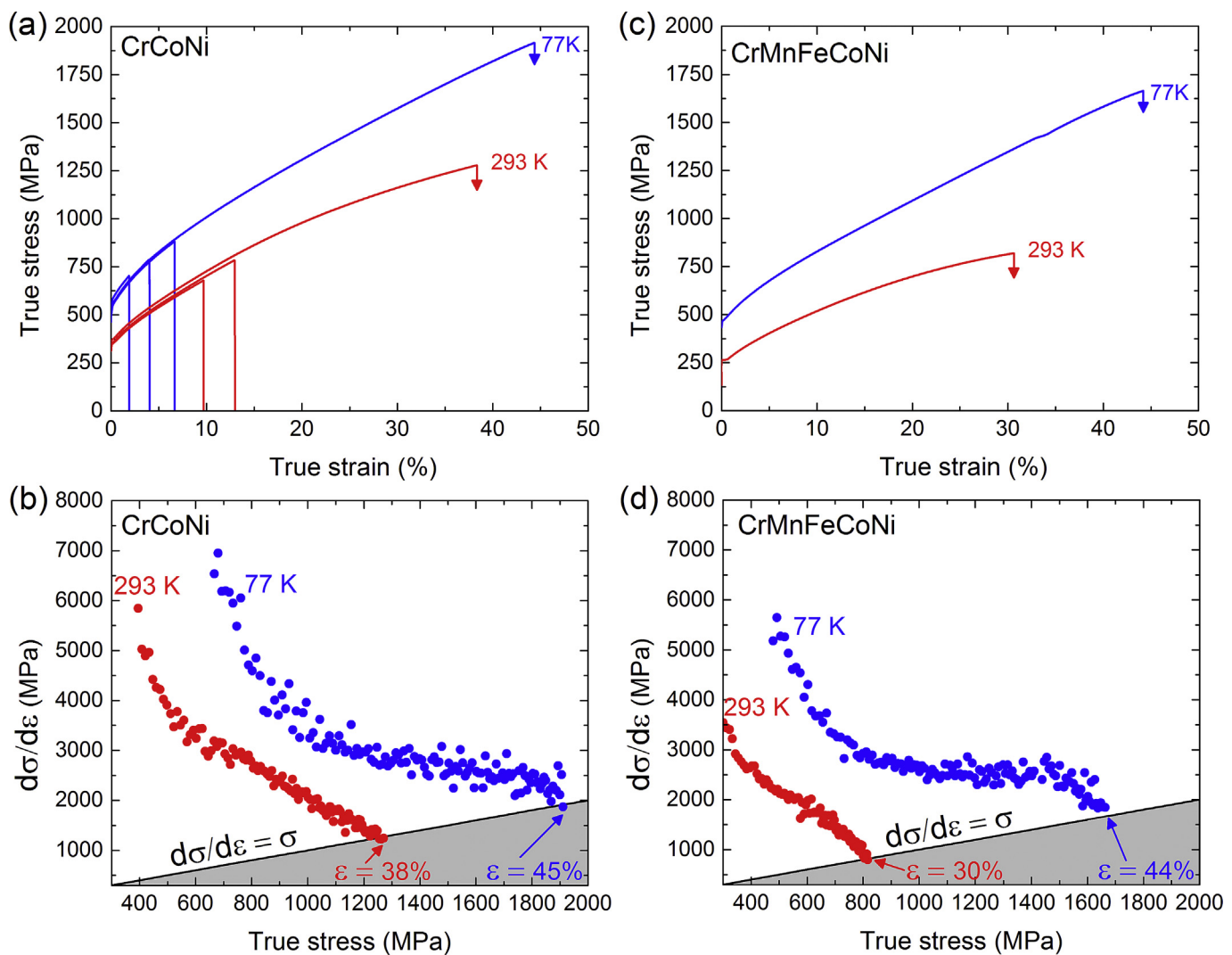


**Fig. 4.** True stress-strain curves of tensile tests at 77 K and 293 K of (a) CrCoNi medium-entropy alloy and (c) CrMnFeCoNi high-entropy alloy. Curves with arrows at the end are from specimens tested to fracture while the other curves in (a) are from interrupted tests. Work hardening rate ( $d\sigma/d\varepsilon$ ) versus true stress of (b) CrCoNi and (d) CrMnFeCoNi.

which is the work hardening rate (WHR), is shown in Fig. 4b as a function of true stress. The grey area indicates the region in which

necking is predicted to occur according to Considère's criterion:  $d\sigma/d\varepsilon < \sigma$ . At 77 K, the WHR is consistently higher than at 293 K and its

intersection with the necking line ( $d\sigma/d\varepsilon = \sigma$ ) occurs at higher strain. As a consequence of the postponement of necking, the ductility at 77 K is higher than at 293 K. Two stages can be distinguished in both WHR curves (Fig. 4b) with an initial rapid decrease followed by a slower second stage. The extended region of work hardening at 77 K compared to 293 K is due to the earlier onset of nanotwinning, as discussed later. For comparison, the previously reported [16] true stress – true strain curves of the CrMnFeCoNi alloy, and its work hardening rate as a function of true stress, are shown in Figs. 4c and d, respectively.

### 3.3. Dislocation analysis

Burgers vector analysis based on the  $\mathbf{g} \cdot \mathbf{b} = 0$  technique in a specimen deformed in compression to 4% true strain is shown in Fig. 5. As expected for FCC materials [37], long dislocations lying in a

(111) plane almost parallel to the TEM foil can be observed in the scanning TEM image (Fig. 5a) obtained in multi-beam condition, see diffraction pattern in Fig. 5b. The white dashed rectangle in Fig. 5a is shown magnified in the g(3g) weak beam micrographs in Figs. 5c–e where three independent  $\langle 220 \rangle$ -type  $\mathbf{g}$  vectors were used for the Burgers vector analysis. Figs. 5c–e reveal the dissociation of a full  $1/2[1 \bar{1} 0]$  dislocation into two Shockley partials according to the following dislocation reaction

$$1/2[1 \bar{1} 0] = 1/6[2 \bar{1} \bar{1}] + 1/6[1 \bar{2} 1] \quad (6)$$

Consistent with the above dissociation scheme, for  $\mathbf{g} [\bar{2} 2 0]$  (Fig. 5e), which is parallel to the Burgers vector of the full dislocation, both partials are visible; for  $\mathbf{g} [0 \bar{2} 2]$  (Fig. 5c), the  $1/6[2 \bar{1} \bar{1}]$  partial is invisible ( $\mathbf{g} \cdot \mathbf{b} = 0$ ) while the other  $1/6[1 \bar{2} 1]$  is visible; and for  $\mathbf{g} [\bar{2} 0 2]$  (Fig. 5d) the  $1/6[2 \bar{1} \bar{1}]$  partial is visible

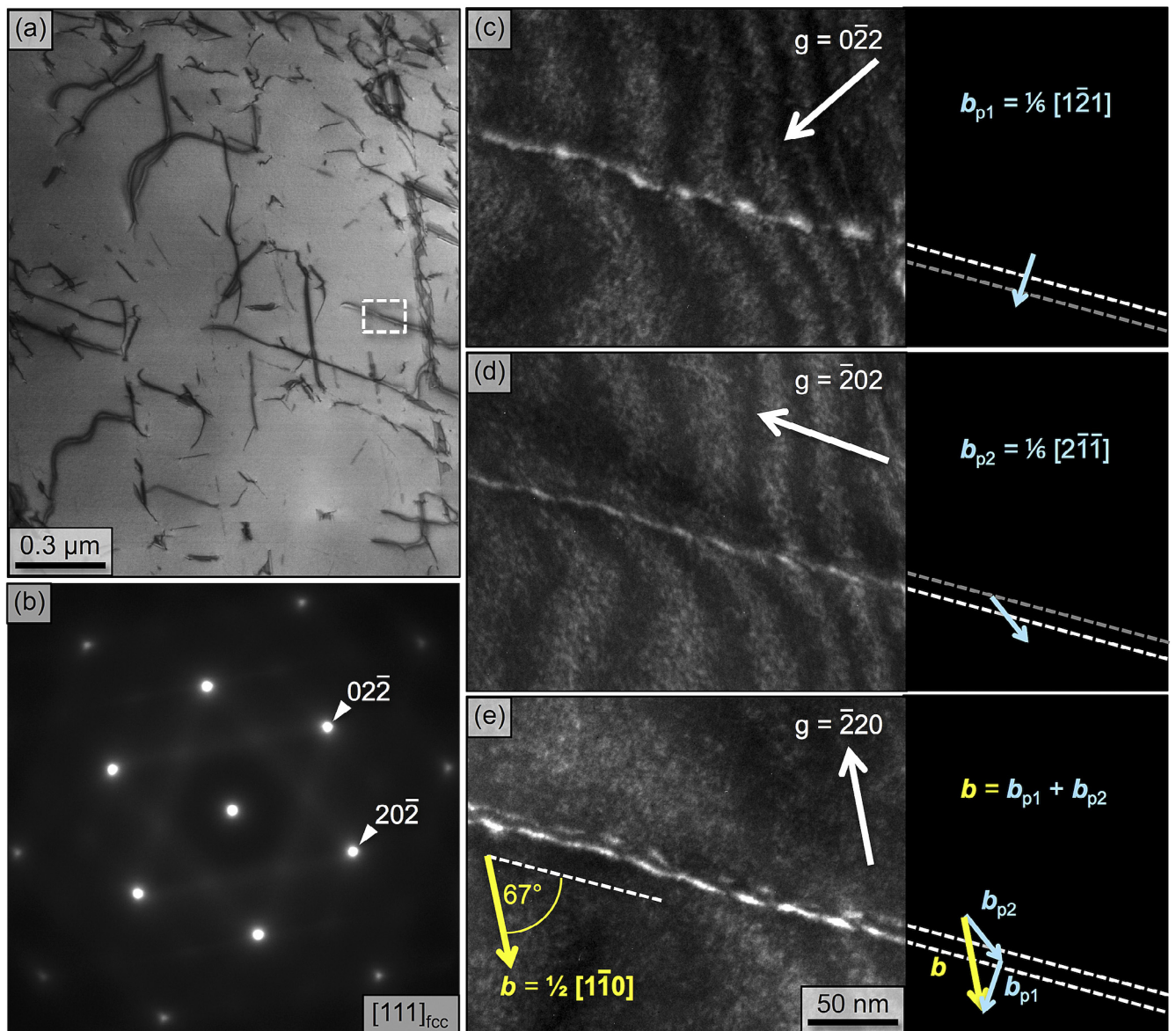


**Fig. 5.** Dislocation analysis after compression at 293 K to 4% true strain. (a) STEM image obtained using the diffraction condition shown in (b) revealing long dislocations lying in the (111) plane almost parallel to the TEM foil. (b) Diffraction pattern showing that the [111] zone-axis is almost parallel to the incident beam. (c–e) g(3g) Weak beam micrographs obtained from the area marked with a white dashed rectangle in (a). The  $\mathbf{g}$  vectors used to set up the g(3g) diffraction condition are indicated with white arrows at the top of each image.

while the other  $1/6[1 \bar{2} 1]$  is invisible.

### 3.4. Stacking fault energy

The separation distance between Shockley partials was measured using images like that shown in Fig. 5e. From these measurements, the actual separation distance  $d_{act}$  was calculated using Eqs. (2)–(4), and the results are plotted in Fig. 6 as a function of the angle  $\beta$  between the dislocation line and the Burgers vector of the full dislocation. The error bars in Fig. 6 represent  $\pm 1$  standard deviation corresponding to at least four distinct measurements at different points along straight segments of isolated dislocations. Eq. (5) was fitted to the experimental data points using the method of weighted least squares, yielding a SFE of  $22 \pm 4 \text{ mJ m}^{-2}$ , see red and black dashed lines in Fig. 6. This value is comparable to those obtained using the weak beam technique in binary  $\text{Co}_{94}\text{Fe}_6$ ,  $\text{Co}_{68}\text{Ni}_{32}$  [38], and the TWIP (twinning induced plasticity) steels  $\text{Fe}_{66}\text{Mn}_{24}\text{Al}_5\text{Si}_5$  [39] and  $\text{Fe}_{69}\text{Cr}_{20}\text{Ni}_{11}$  [40] (compositions in at.%), but lower than the value of  $30 \pm 5 \text{ mJ m}^{-2}$  obtained in the CrMnFeCoNi HEA [20].

### 3.5. Microstructural evolution with strain at 293 K and 77 K

To obtain a better understanding of the governing deformation mechanisms, we analyzed the microstructures of specimens strained to different levels. Representative images showing the microstructural evolution at 293 K and 77 K are provided in Figs. 7 and 8, respectively, where the pictures in the left column are low-magnification BF micrographs, those in the middle column are higher magnification BF (Fig. 7a and Figs. 8a–b) or dark field (DF) (Figs. 7b–c and Figs. 8c–d) micrographs, and those in the right column are selected area diffraction (SAD) patterns (Figs. 7a–c and Figs. 8c–d). When deformation twins were detected, they were imaged edge-on under DF conditions and the diffraction spots used for imaging are circled in red in the corresponding SAD patterns (Figs. 7b–c and Figs. 8c–d).

After 9.7% true strain at 293 K (Fig. 7a), there is a strong increase in dislocation density relative to the unstrained state (Fig. 3) as well as extended SFs, which will be discussed in section 3.7. Plasticity occurs by dislocation glide on several different  $\{111\}$  planes. This observation is in good agreement with previous studies on concentrated FCC solid solutions [37]. Dislocations are found to

pile-up against grain boundaries, which hinder dislocation transmission. Since the  $1/2<110>$  dislocations are dissociated into relatively widely separated  $1/6<112>$  Shockley partials with stacking faults in between, cross slip is hampered and dislocation glide occurs on well-defined  $\{111\}$  planes. An increase in plastic strain from 9.7 to 12.9% at 293 K results in the activation of a second deformation mechanism, deformation twinning, as shown in Fig. 7b. At a much higher strain of 38.3% (in the fractured specimen), the volume fraction of twins is significantly greater and several intersecting twins are present within the grains as shown in the low-magnification BF micrograph in Fig. 7c. Larger strains also result in higher dislocation densities and their organization into cell structures as shown in the inset of Fig. 7c.

Fig. 8 summarizes the microstructural evolution during deformation at 77 K. As at room temperature, the initial stage of plastic deformation is characterized by dislocation glide on  $<110>\{111\}$  slip systems (Figs. 8a–b) with the formation of dislocation pile-ups at the grain boundaries, see lower left corner of Fig. 8b, and by the formation of extended SFs. However, deformation twinning starts at lower plastic strain at 77 K than 293 K. Thus, while deformation twinning was first detected after 12.9% true strain at 293 K, it is present in specimens strained to 6.7% at 77 K, Fig. 8c. Finally, as in the case of the ruptured 293-K specimen (Fig. 7c), at 77 K also the ruptured specimen (44.2% true strain) contains several intersecting twins, Fig. 6d.

The nature of the stacking faults (intrinsic versus extrinsic) was assessed as follows. Fig. 9 shows wide stacking faults exhibiting fringe contrast in a specimen subjected to 6.7% true strain at 77 K. The stacking faults are intersected by nanotwins indicated with red arrows in Fig. 9a. The character of the stacking fault was determined using a procedure developed for FCC materials [28]. When the origin of a  $\mathbf{g}$  vector of type  $\langle 111 \rangle$ ,  $\langle 220 \rangle$  or  $\langle 400 \rangle$  is placed at the center of the stacking fault in the DF micrograph ( $\mathbf{g}[111]$  in Fig. 9b), it points away from the bright outer fringe if the fault is intrinsic and toward it if it is extrinsic. The reverse correlation occurs if the reflections are  $\langle 200 \rangle$ ,  $\langle 222 \rangle$  or  $\langle 440 \rangle$ . As the  $\mathbf{g}[111]$  vector is pointing away from the bright outer fringe, it is concluded that the stacking faults in Fig. 9b are intrinsic rather than extrinsic.

### 3.6. Critical twinning stress

Based on the above microstructural observations we conclude that twinning starts at true strains between 4.0% and 6.7% at 77 K and between 9.7% and 12.9% at 293 K. The corresponding true stress values, hereafter referred to as the twinning stress values, are  $835 \pm 55 \text{ MPa}$  at 77 K and  $740 \pm 45 \text{ MPa}$  at 293 K. Given the overlap in these values and the experimental scatter, we consider the roughly temperature-independent twinning stress to be  $\sim 790 \pm 100 \text{ MPa}$ . Assuming a Taylor factor of 3.06, the critical resolved shear stress for twinning can then be estimated as  $260 \pm 30 \text{ MPa}$ . This value is comparable to that determined in the CrMnFeCoNi HEA with the same grain size:  $235 \pm 10 \text{ MPa}$  [16]. Different models [41–50] have been proposed for the prediction of the critical twinning stress in FCC materials, which depends on factors such as SFE, grain size, and shear modulus (among others). Here we kept the grain size constant so it need not be considered as a contributing factor. However, further studies are needed to understand how the other factors interact to produce roughly similar twinning stresses in CrCoNi and CrMnFeCoNi. Regardless, what can be concluded is that the twinning stress is more easily reached in CrCoNi (present study) than in CrMnFeCoNi [16]. This is because of two reasons. First, the yield stress of CrCoNi is significantly higher than that of CrMnFeCoNi: 360 MPa versus 265 MPa at 293 K and 560 MPa versus 460 MPa at 77 K, see Fig. 4. This has been explained using a new theory of solid solution strengthening that takes into

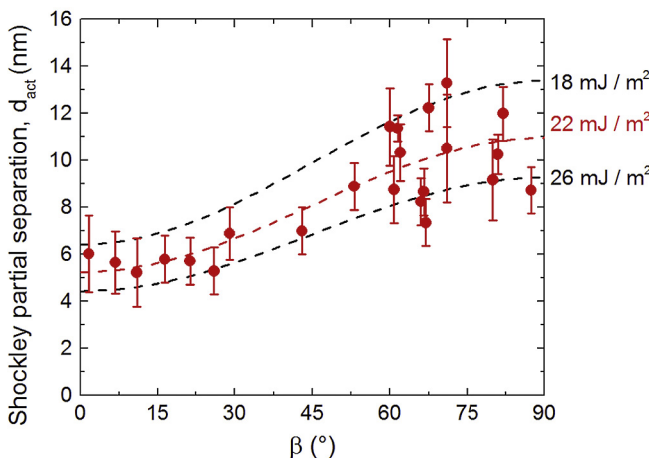
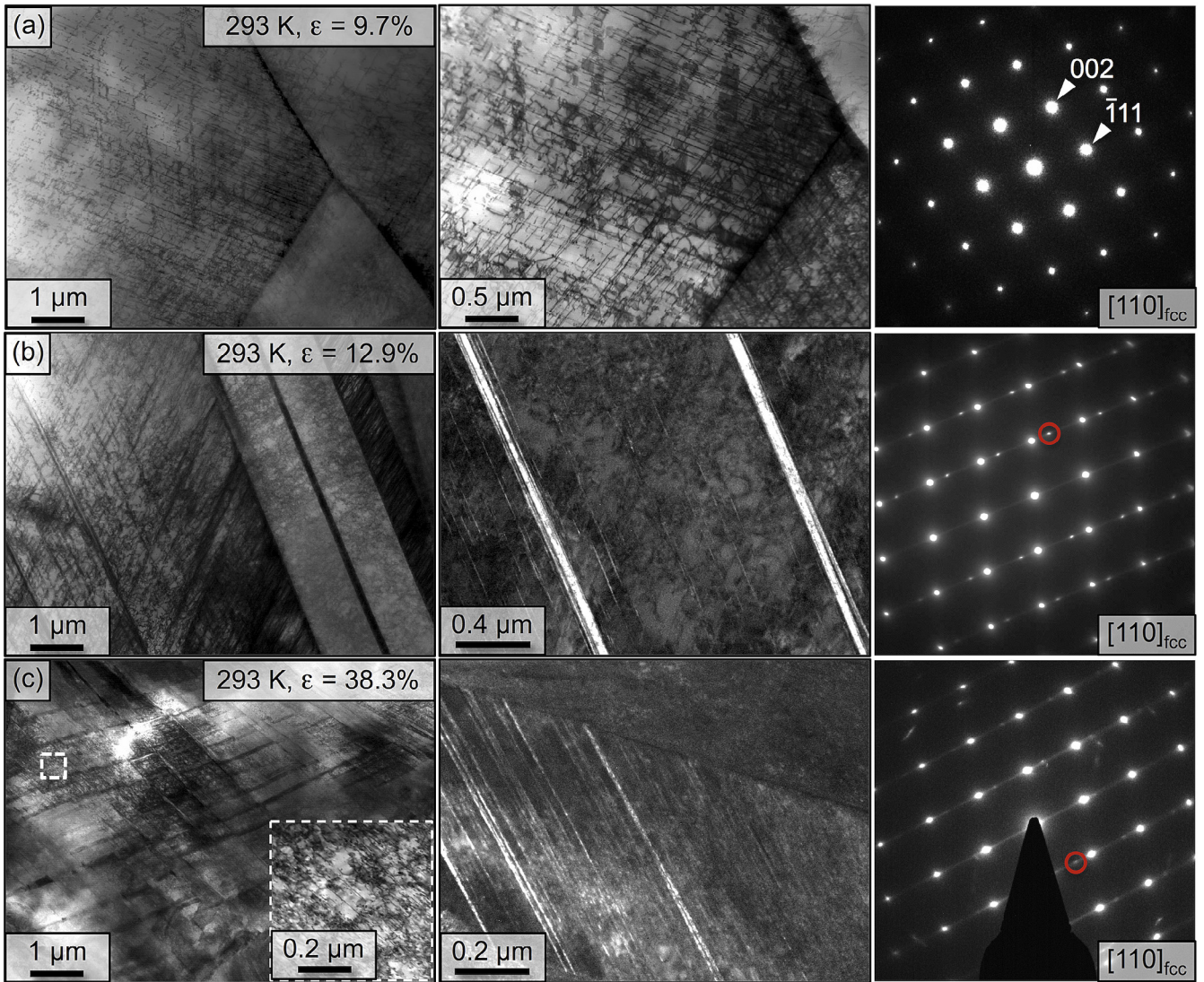


Fig. 6. Spacing between Shockley partial dislocations as a function of the angle between the dislocation line and the Burgers vector of the full dislocation. The dashed lines represent partial dislocation spacings calculated using Eq. (5) for different stacking fault energies indicated on the right side of the figure.



**Fig. 7.** TEM micrographs showing microstructural evolution with true tensile strain at 293 K. Figures in the left column are low magnification BF images, those in the middle are either (a) BF or (b–c) DF images, and those in the right column are SAD patterns. Diffraction spots circled in red in the SAD patterns (b–c) were used to obtain the corresponding DF images where nanotwins are observed edge-on. (For interpretation of the references to colour in this figure legend, the reader is referred to the web version of this article.)

account atomic volume misfits in concentrated solid solutions [17]. The compositional dependence of yield stress has also been correlated with the mean square atomic displacements of the constituent atoms from their ideal FCC lattice positions and shown to be higher in CrCoNi than in CrMnFeCoNi [51]. Second, the work hardening rate is higher in CrCoNi than in CrMnFeCoNi, which is mainly due to the fact that the shear modulus of the former (87 GPa [4]) is larger than that of the latter (81 GPa [36]). The earlier activation of twinning means that there is a larger strain range where nanotwinning can occur in CrCoNi which then results in superior mechanical properties. Another noteworthy result is that, in both alloys, the yield stress increases with decreasing temperature but the twinning stress is relatively insensitive to temperature. Consequently, the twinning stress is reached more easily (i.e., at lower strains) at 77 K than at 293 K and the mechanical properties of both alloys improve at cryogenic temperatures.

### 3.7. Further features of microstructure prior to the onset of twinning

Fig. 10 shows some interesting microstructural features in a

specimen deformed in tension at 293 K to a true strain of 9.7%. Fig. 10a shows a network of extended and contracted nodes, which further confirms the low SFE measured in the present study since networks of extended and contracted nodes are frequently observed in relatively low SFE materials [52] as a result of intersections of dissociated dislocations [53]. Fig. 10b also reveals the presence of extended SFs on different {111} planes that intersect each other. One set of SFs is edge-on (white arrowheads in Fig. 10b), which produce the streaks observed in the diffraction pattern on the right side of Fig. 10b; they intersect another set of SFs that are more in plane (indicated by the red arrowheads). Stacking faults that are sheared during deformation typically leave behind interfacial partial dislocations [54]. These interfacial dislocations may be mobile and their glide may result in thickening or thinning of the SF. Further interactions may lead to two intrinsic SFs forming on successive {111} planes producing first an extrinsic SF [55] and ultimately a nanotwin when three or more intrinsic SFs form on successive {111} planes. An example of extended SFs (bright and dark fringes) which intersect edge-on nanotwins is shown in Fig. 9. Based on these observations, it is therefore likely that the formation of extended SFs plays a key role in the formation of twins as

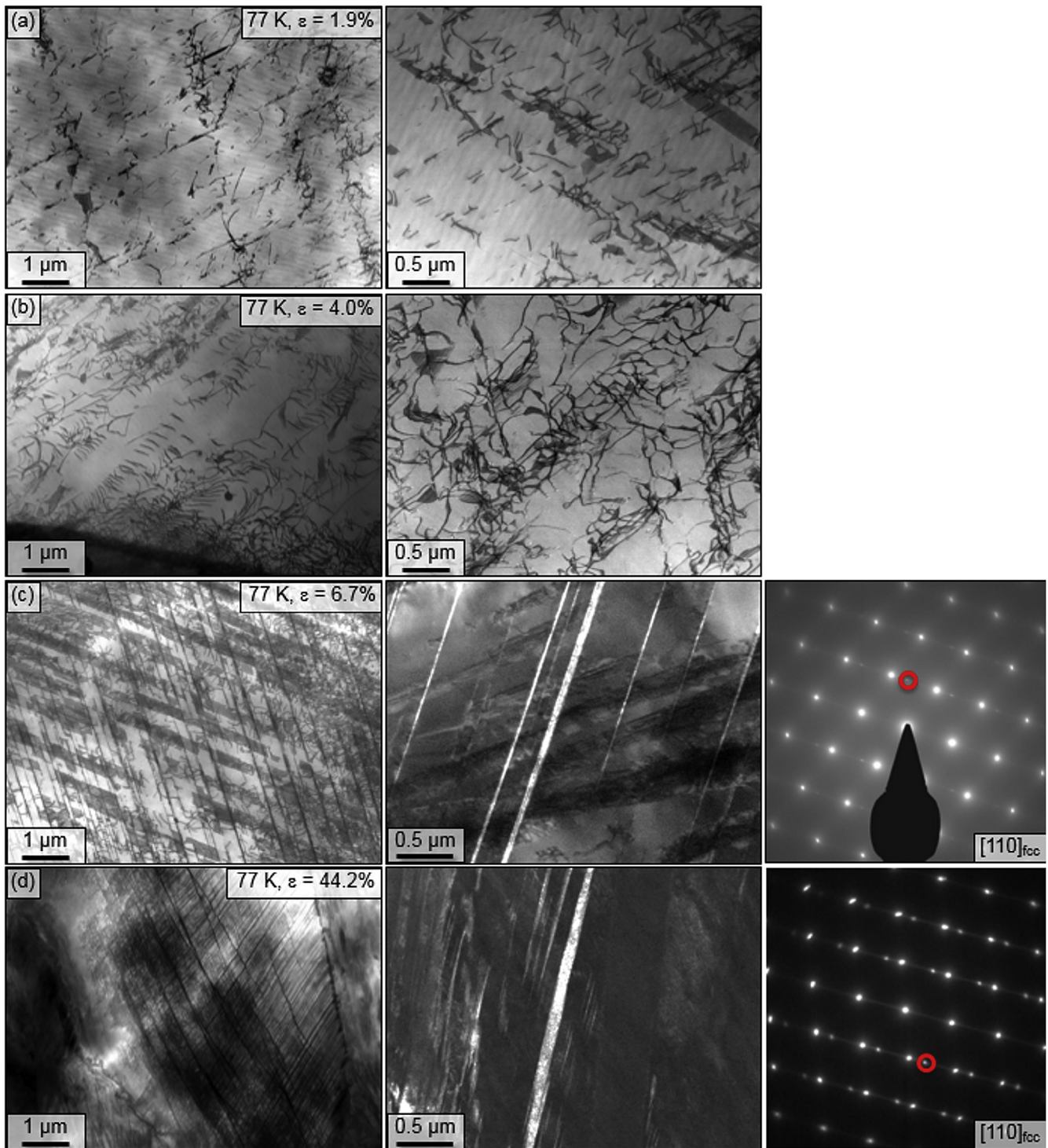


**Fig. 8.** TEM micrographs showing microstructural evolution with true tensile strain at 77 K. In (a) and (b) both rows are BF images. In (c) and (d) figures in the left column are BF images, those in the middle are DF images, and those in the right column are SAD patterns showing diffraction spots from the twin and matrix. Diffraction spots circled in red in the SAD patterns were used to obtain the dark field images. (For interpretation of the references to colour in this figure legend, the reader is referred to the web version of this article.)

suggested by many authors in the literature, e.g., in Cu-based alloys [56], and TWIP and Hadfield steels [50,57,58].

#### 4. Summary and conclusions

An equiatomic CrCoNi medium-entropy alloy was produced by vacuum induction melting and casting followed by swaging at

room temperature and recrystallization at 1173 K for 1 h. This thermomechanical process yielded a FCC single-phase material with a uniform grain size of ~16 μm and close to random texture. Its mechanical properties were investigated at 77 K and 293 K and the governing deformation mechanisms characterized by TEM. Based on a comparison of the present results with those from earlier studies on the CrMnFeCoNi HEA, the following conclusions can be

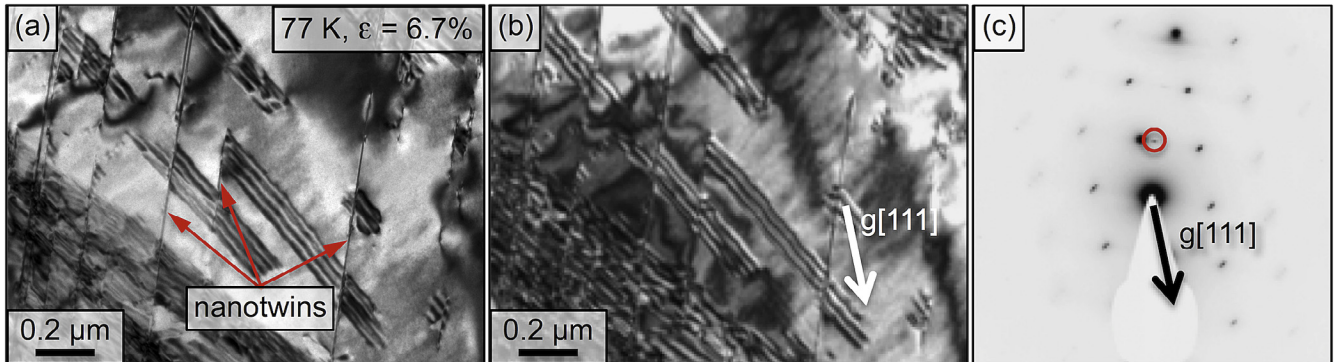


**Fig. 9.** (a) BF micrograph showing edge-on twins intersected by extended stacking faults (black and white fringes). (b) DF micrograph. (c) Diffraction pattern showing the presence of extra diffraction spots (circled in red) due to the presence of edge-on deformation twins. (For interpretation of the references to colour in this figure legend, the reader is referred to the web version of this article.)

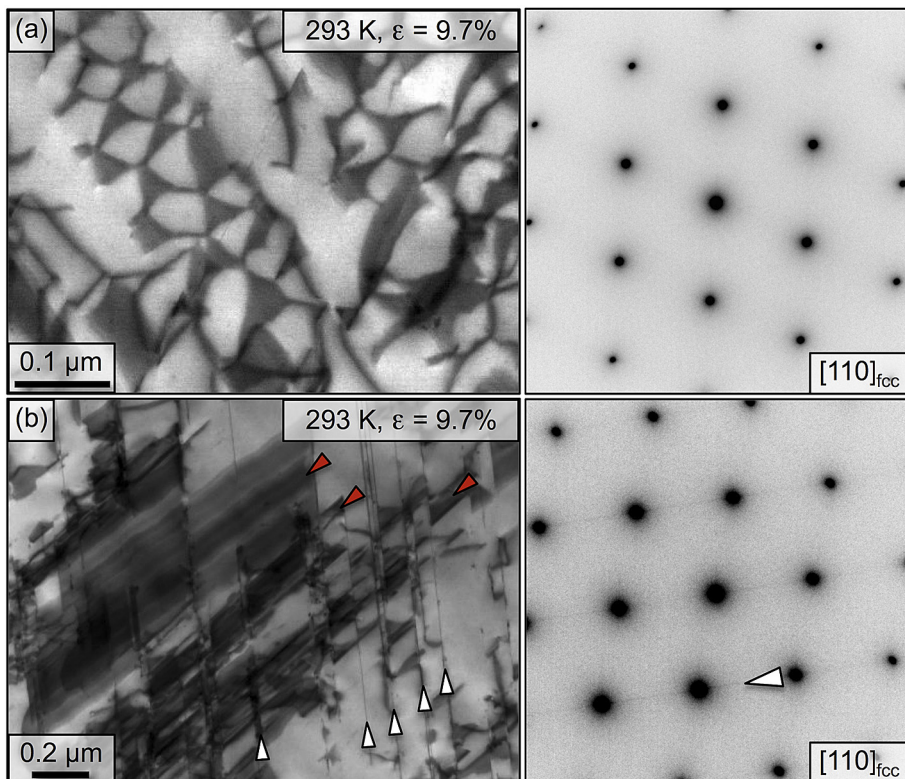


**Fig. 10.** Interesting microstructural features observed prior to mechanical twinning. (a) Network of in-plane dislocations showing extended nodes (left image) and corresponding diffraction pattern (right image). (b) Intersections of two families of SFs (left image): SFs of the 1st family are edge-on and are indicated by white arrowheads at the bottom of Fig. 10b whereas SFs of the 2nd family are close to in-plane and are indicated by red arrowheads. The corresponding diffraction pattern shows streaks (white arrowhead) perpendicular to edge-on SFs. Negative images of the diffraction patterns are shown to highlight (a) absence or (b) presence of streaks due to edge-on stacking faults. (For interpretation of the references to colour in this figure legend, the reader is referred to the web version of this article.)

drawn.

- (1) The yield strength, work hardening rate, ultimate tensile strength, and elongation to fracture of the CrCoNi MEA all increase strongly with decreasing temperature, similar to what has been observed before in the CrMnFeCoNi HEA [16]. However, the mechanical properties of the CrCoNi MEA are superior to those of the CrMnFeCoNi HEA. Both alloys were processed similarly to have close to random texture and practically identical grain sizes, so the difference in mechanical behavior must be due to other reasons.

- (2) The initial stage of plasticity in CrCoNi is characterized by the glide of  $1/2<110>$  dislocations dissociated into two  $1/6<112>$  Shockley partials on  $\{111\}$  planes with a stacking fault in between, similar to the behavior of CrMnFeCoNi.
- (3) The separation between the Shockley partials in CrCoNi ranges from ~5 nm near the screw orientation to ~11 nm near the edge, which is larger than the corresponding partial separations in CrMnFeCoNi, ~4 and ~6.5 nm, respectively [20]. These relatively wide dissociations are expected to hamper cross-slip and promote planar slip in the early stages of plastic deformation in both alloys.

- (4) From the measured partial separations, the stacking fault energy of CrCoNi can be estimated to be  $22 \pm 4 \text{ mJ m}^{-2}$ , which is approximately 25% lower than that determined previously for CrMnFeCoNi ( $30 \pm 5 \text{ mJ m}^{-2}$ ) [20].
- (5) As deformation progresses, nanotwinning is activated as an additional deformation mechanism in CrCoNi at true strains between 4.0% and 6.7% at 77 K and between 9.7% and 12.9% at 293 K. This is earlier than in CrMnFeCoNi [16]. Twinning promotes a high work hardening rate by introducing extra boundaries that act as barriers to dislocation motion (“dynamic Hall-Petch effect”), which postpones the onset of necking and increases ductility.
- (6) The true tensile stress and resolved shear stress for the onset of twinning in CrCoNi are determined to be  $790 \pm 100 \text{ MPa}$  and  $260 \pm 30 \text{ MPa}$ , respectively, roughly independent of temperature. For the same grain size, the corresponding twinning stresses in CrMnCoFeNi were previously found to be comparable:  $720 \pm 30 \text{ MPa}$  and  $235 \pm 10 \text{ MPa}$ , respectively [16].
- (7) There are at least two reasons why the ultimate strength and ductility of the CrCoNi MEA are higher than those of the CrMnFeCoNi HEA: its yield strength and work hardening rate are higher, which allow the twinning stress to be reached earlier (after smaller plastic strains) and nanotwinning to occur over a more extended strain range. This in turn allows the necking instability to be postponed more effectively in CrCoNi than in CrMnFeCoNi and the strength-ductility combination to be better.
- (8) The critical stress for twinning in both alloys is roughly independent of temperature, but their yield strengths increase with decreasing temperature. This makes it easier to reach the twinning stress as the temperature is lowered. Therefore, nanotwinning occurs over a more extended strain range, allowing the necking instability to be postponed and the strength-ductility combination to improve as the temperature is decreased in both alloys.

## Acknowledgments

G.L., E.P.G., and G.E. acknowledge funding from the German Research Foundation (DFG) through projects LA 3607/1-1, GE 2736/1-1, and project B7 of the SFB/TR 103, respectively.

## References

- [1] J.-W. Yeh, Physical metallurgy of high-entropy alloys, *JOM* 67 (2015) 2254.
- [2] A. Gali, E.P. George, Tensile properties of high- and medium-entropy alloys, *Intermetallics* 39 (2013) 74.
- [3] Z. Wu, H. Bei, F. Otto, G.M. Pharr, E.P. George, Recovery, recrystallization, grain growth and phase stability of a family of FCC-structured multi-component equiatomic solid solution alloys, *Intermetallics* 46 (2014) 131.
- [4] Z. Wu, H. Bei, G.M. Pharr, E.P. George, Temperature dependence of the mechanical properties of equiatomic solid solution alloys with face-centered cubic crystal structures, *Acta Mater.* 81 (2014) 428.
- [5] F. Otto, A. Dlouhý, C. Somsen, H. Bei, G. Eggeler, E.P. George, The influences of temperature and microstructure on the tensile properties of a CoCrFeMnNi high-entropy alloy, *Acta Mater.* 61 (2013) 5743.
- [6] B. Gludovatz, A. Hohenwarter, K.V.S. Thurston, H. Bei, Z. Wu, E.P. George, R.O. Ritchie, Exceptional damage-tolerance of a medium-entropy alloy CrCoNi at cryogenic temperatures, *Nat. Commun.* 7 (2016).
- [7] B. Gludovatz, A. Hohenwarter, D. Cattoor, E.H. Chang, E.P. George, R.O. Ritchie, A fracture-resistant high-entropy alloy for cryogenic applications, *Science* 345 (2014) 1153.
- [8] C. Zhu, Z.P. Lu, T.G. Nieh, Incipient plasticity and dislocation nucleation of FeCoCrNiMn high-entropy alloy, *Acta Mater.* 61 (2013) 2993.
- [9] G.A. Salishchev, M.A. Tikhonovsky, D.G. Shaysultanov, N.D. Stepanov, A.V. Kuznetsov, I.V. Kolodiy, A.S. Tortika, O.N. Senkov, Effect of Mn and V on structure and mechanical properties of high-entropy alloys based on CoCrFeNi system, *J. Alloys Compd.* 591 (2014) 11.
- [10] J.Y. He, C. Zhu, D.Q. Zhou, W.H. Liu, T.G. Nieh, Z.P. Lu, Steady state flow of the FeCoNiCrMn high entropy alloy at elevated temperatures, *Intermetallics* 55 (2014) 9.
- [11] C.C. Tasan, Y. Deng, K.G. Pradeep, M.J. Yao, H. Springer, D. Raabe, Composition dependence of phase stability, deformation mechanisms, and mechanical properties of the CoCrFeMnNi high-entropy alloy system, *JOM* 66 (2014) 1993.
- [12] N. Stepanov, M. Tikhonovsky, N. Yurchenko, D. Zyabkin, M. Klimova, S. Zherebtsov, A. Efimov, G. Salishchev, Effect of cryo-deformation on structure and properties of CoCrFeNiMn high-entropy alloy, *Intermetallics* 59 (2015) 8.
- [13] Z. Zhang, M.M. Mao, J. Wang, B. Gludovatz, Z. Zhang, S.X. Mao, E.P. George, Q. Yu, R.O. Ritchie, Nanoscale origins of the damage tolerance of the high-entropy alloy CrMnFeCoNi, *Nat. Commun.* 6 (2015).
- [14] W. Woo, E.W. Huang, J.-W. Yeh, H. Choo, C. Lee, S.-Y. Tu, In-situ neutron diffraction studies on high-temperature deformation behavior in a CoCrFeMnNi high entropy alloy, *Intermetallics* 62 (2015) 1.
- [15] T.M. Smith, M.S. Hooshmand, B.D. Esser, F. Otto, D.W. McComb, E.P. George, M. Ghazisaeidi, M.J. Mills, Atomic-scale characterization and modeling of  $60^\circ$  dislocations in a high-entropy alloy, *Acta Mater.* 110 (2016) 352.
- [16] G. Laplanche, A. Kostka, O.M. Horst, G. Eggeler, E.P. George, Microstructure evolution and critical stress for twinning in the CrMnFeCoNi high-entropy alloy, *Acta Mater.* 118 (2016) 152.
- [17] C. Varvenne, A. Luque, W.A. Curtin, Theory of strengthening in fcc high-entropy alloys, *Acta Mater.* 118 (2016) 164.
- [18] Z. Li, K.G. Pradeep, Y. Deng, D. Raabe, C.C. Tasan, Metastable high-entropy dual-phase alloys overcome the strength-ductility trade-off, *Nature* 534 (2016) 227.
- [19] H.S. Oh, D. Ma, G.P. Leyson, B. Grabowski, E.S. Park, F. Körmann, D. Raabe, Lattice distortions in the FeCoNiCrMn high entropy alloy studied by theory and experiment, *Entropy* 18 (2016) 321.
- [20] N.L. Okamoto, S. Fujimoto, Y. Kambara, M. Kawamura, Z.M. Chen, H. Matsunoshita, K. Tanaka, H. Inui, E.P. George, Size effect, critical resolved shear stress, stacking fault energy, and solid solution strengthening in the CrMnFeCoNi high-entropy alloy, *Sci. Rep.* 6 (2016).
- [21] Y. Liu, J. Wang, Q. Fang, B. Liu, Y. Wu, S. Chen, Preparation of superfine-grained high entropy alloy by spark plasma sintering gas atomized powder, *Intermetallics* 68 (2016) 16.
- [22] D.-H. Lee, M.-Y. Seok, Y. Zhao, I.-C. Choi, J. He, Z. Lu, J.-Y. Suh, U. Ramamurthy, M. Kawasaki, T.G. Langdon, J.-i. Jang, Spherical nanoindentation creep behavior of nanocrystalline and coarse-grained CoCrFeMnNi high-entropy alloys, *Acta Mater.* 109 (2016) 314.
- [23] B. Wang, A. Fu, X. Huang, B. Liu, Y. Liu, Z. Li, X. Zan, Mechanical properties and microstructure of the CoCrFeMnNi high entropy alloy under high strain rate compression, *J. Mater. Eng. Perform.* 25 (2016) 2985.
- [24] G. Laplanche, O. Horst, F. Otto, G. Eggeler, E.P. George, Microstructural evolution of a CoCrFeMnNi high-entropy alloy after swaging and annealing, *J. Alloys Compd.* 647 (2015) 548.
- [25] G. Laplanche, U.F. Volkert, G. Eggeler, E.P. George, Oxidation behavior of the CrMnFeCoNi high-entropy alloy, *Oxid. Metals* 85 (2016) 629.
- [26] P.M. Kelly, A. Jostsons, R.G. Blake, J.G. Napier, The determination of foil thickness by scanning transmission electron microscopy, *Phys. Status Solidi (a)* 31 (1975) 771.
- [27] S.M. Allen, Foil thickness measurements from convergent-beam diffraction patterns, *Philos. Mag. A* 43 (1981) 325.
- [28] D.B. Williams, C.B. Carter, *Transmission Electron Microscopy: a Textbook for Materials Science*, Springer, US, Boston, MA, 1996.
- [29] D.J.H. Cockayne, The weak-beam technique as applied to dissociation measurements, *J. de Physique Colloques* C7 35 (1974) 141.
- [30] D.J.H. Cockayne, A theoretical analysis of the weak-beam method of electron microscopy, *Z. für Naturforsch.* 27a (1972) 452.
- [31] R. Dr Ridder, S. Amelinckx, Approximate theoretical treatment of weak-beam dislocation images, *Phys. Status Solidi (b)* 48 (1971) 541.
- [32] F. Otto, N.L. Hanold, E.P. George, Microstructural evolution after thermo-mechanical processing in an equiatomic, single-phase CoCrFeMnNi high-entropy alloy with special focus on twin boundaries, *Intermetallics* 54 (2014) 39.
- [33] A.T. English, G.Y. Chin, On the variation of wire texture with stacking fault energy in f.c.c. metals and alloys, *Acta Metall.* 13 (1965) 1013.
- [34] D.N. Lee, Y.H. Chung, M.C. Shin, Preferred orientation in extruded aluminium alloy rod, *Scr. Metall.* 17 (1983) 339.
- [35] H.J. Shin, H.T. Jeong, D.N. Lee, Deformation and annealing textures of silver wire, *Mater. Sci. Eng. A* 279 (2000) 244.
- [36] G. Laplanche, P. Gadaud, O. Horst, F. Otto, G. Eggeler, E.P. George, Temperature dependencies of the elastic moduli and thermal expansion coefficient of an equiatomic, single-phase CoCrFeMnNi high-entropy alloy, *J. Alloys Compd.* 623 (2015) 348.
- [37] R.W.K. Honeycombe, *The Plastic Deformation of Metals*, second ed., Edward Arnold Ltd, London, 1984.
- [38] T.C. Tisone, The concentration and temperature dependence of the stacking fault energy in face-centered cubic Co-Fe alloys, *Acta Metall.* 21 (1973) 229.
- [39] D.T. Pierce, J.A. Jiménez, J. Bentley, D. Raabe, J.E. Wittig, The influence of stacking fault energy on the microstructural and strain-hardening evolution of Fe–Mn–Al–Si steels during tensile deformation, *Acta Mater.* 100 (2015) 178.
- [40] J. Lu, L. Hultman, E. Holmström, K.H. Antonsson, M. Grehk, W. Li, L. Vitos, A. Golpayegani, Stacking fault energies in austenitic stainless steels, *Acta*

- Mater. 111 (2016) 39.
- [41] J.A. Venables, Deformation twinning in face-centred cubic metals, *Philos. Mag.* 6 (63) (1961) 379.
- [42] J.B. Cohen, J. Weertman, A dislocation model for twinning in f.c.c. metals, *Acta Metall.* 11 (1963) 996.
- [43] J.A. Venables, The electron microscopy of deformation twinning, *J. Phys. Chem. Solids* 25 (1964) 685.
- [44] G. Fontaine, Propagation des macles dans les métaux fortement écrouis, *Phys. Status Solidi (b)* 15 (1966) 603.
- [45] S. Mahajan, G.Y. Chin, Formation of deformation twins in f.c.c. crystals, *Acta Metall.* 21 (1973) 1353.
- [46] N. Narita, J. Takamura, Deformation twinning in silver-and copper-alloy crystals, *Philos. Mag.* 29 (1974) 1001.
- [47] H. Fujita, T. Mori, A formation mechanism of mechanical twins in F.C.C. Metals, *Scr. Metall.* 9 (1975) 631.
- [48] J.F.M. Vergnol, J. Grilhé, Relationship between extrinsic stacking faults and mechanical twinning in F.C.C. solid solutions with low stacking fault energy, *J. Phys.* 45 (1984) 1479.
- [49] I. Karaman, H. Sehitoglu, K. Gall, Y.I. Chumlyakov, H.J. Maier, Deformation of single crystal Hadfield steel by twinning and slip, *Acta Mater.* 48 (2000) 1345.
- [50] I. Karaman, H. Sehitoglu, Y.I. Chumlyakov, H.J. Maier, I.V. Kireeva, Extrinsic stacking faults and twinning in hadfield manganese steel single crystals, *Scr. Mater.* 44 (2001) 337.
- [51] N.L. Okamoto, K. Yuge, K. Tanaka, H. Inui, E.P. George, Atomic displacement in the CrMnFeCoNi high-entropy alloy—A scaling factor to predict solid solution strengthening, *AIP Adv.* 6 (2016) 125008.
- [52] P.C.J. Gallagher, J. Washburn, The formation of extrinsic-intrinsic faulting, *Philos. Mag.* 15 (1967) 969.
- [53] M.J. Whelan, Dislocation interactions in face-centred cubic metals, with particular reference to stainless steel, *Proc. R. Soc. Lond. A Math. Phys. Eng. Sci.* 249 (1959) 114.
- [54] L. Rémy, The interaction between slip and twinning systems and the influence of twinning on the mechanical behavior of fcc metals and alloys, *Metall. Trans. A* 12 (1981) 387.
- [55] J.P. Hirth, J. Lothe, *Theory of Dislocations*, John Wiley & Sons, New York, 1982.
- [56] F. Tranchant, J. Vergnol, M.F. Denanot, J. Grilhé, Mechanical twinning mechanisms in Cu-Al crystals with very low stacking fault energy, *Scr. Metall.* 21 (1987) 269.
- [57] H. Idrissi, L. Ryelandt, M. Veron, D. Schryvers, P.J. Jacques, Is there a relationship between the stacking fault character and the activated mode of plasticity of Fe–Mn-based austenitic steels? *Scr. Mater.* 60 (2009) 941.
- [58] H. Idrissi, K. Renard, L. Ryelandt, D. Schryvers, P.J. Jacques, On the mechanism of twin formation in Fe–Mn–C TWIP steels, *Acta Mater.* 58 (2010) 2464.